osteology

MDPI

Case Report

Persistent Bone-to-Implant Contact in Denosumab-Associated MRONJ: A Multimodal Human Retrieval Study

Giovanni Vantaggiato [1,2], Georgios Romanos [3,4], Nicole Riberti [5], Michele Furlani [6], Morena Petrini [7], Tania Vanessa Pierfelice [7], Alessandra Giuliani [8,*], Adriano Piattelli [9] and Giovanna Iezzi [7]

1 Private Practice, 73020 Lecce, Italy; giovannivantaggiato@libero.it
2 Department of Dentistry, Istituto Santa Chiara, 73100 Lecce, Italy
3 Department of Periodontics and Endodontics, School of Dental Medicine, Stony Brook University, Stony Brook, NY 11794, USA; grperio@gmail.com
4 Department of Oral Surgery and Implant Dentistry, Johann Wolfgang Goethe University, Innenstadt II, 60629 Frankfurt am Main, Germany
5 Department of Clinical and Molecular Sciences, Polytechnic University of Marche, 60131 Ancona, Italy; n.riberti@staff.univpm.it
6 Department of Life, Health and Health Professions Sciences, Link Campus University, 00165 Rome, Italy; m.furlani@unilink.it
7 Department of Medical, Oral and Biotechnological Sciences, University G. d'Annunzio of Chieti-Pescara, 66100 Chieti, Italy; morena.petrini@unich.it (M.P.); tania.pierfelice@unich.it (T.V.P.); gio.iezzi@unich.it (G.I.)
8 Department of Odontostomatologic and Specialized Clinical Sciences, Polytechnic University of Marche, 60131 Ancona, Italy
9 Facultad de Medicina, UCAM Universidad Catolica San Antonio de Murcia, 30107 Murcia, Spain; apiattelli51@gmail.com
* Correspondence: a.giuliani@staff.univpm.it

Abstract

Background/Objectives: Evidence on the biological integrity of clinically stable dental implants involved in medication-related osteonecrosis of the jaw (MRONJ) is limited. This single-patient human retrieval study characterized the bone–implant interface within a mandibular sequestrum associated with high-dose denosumab therapy, with particular emphasis on the distinction between persistent bone-to-implant contact and biologically viable osseointegration. **Methods:** A spontaneously exfoliated mandibular sequestrum containing five implants that had remained clinically stable relative to the surrounding bone during earlier phases of MRONJ progression was retrieved from a patient receiving denosumab for metastatic prostate cancer. The specimen was examined by undecalcified histology and histomorphometry. Selected peri-implant and inter-implant bone regions were further evaluated using synchrotron radiation-based phase-contrast microtomography and neural-network-assisted segmentation of osteocyte lacunae. Bone-to-implant contact was quantified over the entire endosseous implant surface (EBIC) and from the first coronal bone contact to the implant apex (FBIC). **Results:** Persistent bone-to-implant contact was present around all five implants despite extensive osteonecrosis. Histology showed non-vital bone, empty osteocyte lacunae, microfractures, bacterial colonization, demineralized areas, Howship-like resorption lacunae without identifiable osteoclasts, and no detectable osteoblastic activity in the examined fields. Mean EBIC was 42.45 ± 13.41%, whereas mean FBIC was 84.40 ± 4.17%, indicating substantial residual physical contact apical to areas of coronal bone loss. In the sampled regions, peri-implant bone showed lower osteocyte lacunar volume and numerical density and broader relative mineralization distributions than inter-implant bone. Because the observations derived from one patient and non-independent anatomical regions, these comparisons are descriptive and hypothesis-generating. **Conclusions:** The clinical stability of an implant relative to the surrounding bone should not be interpreted as evidence of biological integrity of the

Check for updates

Academic Editor: Samo Karel Fokter

Received: 25 July 2026
Revised: 7 September 2026
Accepted: 24 September 2026
Published: 2 October 2026

Copyright: © 2026 by the authors. Licensee MDPI, Basel, Switzerland. This article is an open access article distributed under the terms and conditions of the Creative Commons Attribution (CC BY) license.

peri-implant interface; at advanced stages, implants may become mobile together with the necrotic sequestrum despite retaining substantial histological bone-to-implant contact. Importantly, persistent histomorphometric contact should not be interpreted as evidence of biologically viable or functional osseointegration. These findings highlight a dissociation between the implant clinical stability, physical bone contact, and biological integrity of the peri-implant interface. Multimodal human retrieval analysis may help characterize the microstructural consequences of MRONJ, although the respective contributions of antiresorptive treatment, infection, peri-implant disease, and mechanical loading require investigation in larger, independently validated datasets.

Keywords: medication-related osteonecrosis of the jaw; denosumab; dental implants; osseointegration; peri-implant bone; synchrotron radiation microtomography; osteocyte lacunae; artificial intelligence-assisted segmentation

1. Introduction

The long-term stability of dental implants depends on a dynamic bone–implant interface in which mineralized bone remains structurally connected to the implant surface and biologically capable of remodeling under functional loading. In routine implant dentistry, implant survival is often defined clinically by the persistence of the fixture in situ; however, survival does not necessarily indicate biologically healthy osseointegration when systemic disease, pharmacological suppression of bone turnover, infection, or peri-implant inflammation are present.

Medication-related osteonecrosis of the jaw (MRONJ) is a severe adverse event associated with antiresorptive and antiangiogenic therapies, particularly in patients treated for malignant disease or osteoporosis [1–4]. Denosumab, a monoclonal antibody targeting receptor activator of nuclear factor-kappa B ligand (RANKL), reduces osteoclast formation and activity and is widely used in oncologic skeletal-related event prevention. In the jaws, where bone turnover, microbial challenge, mucosal trauma, and mechanical loading interact, profound suppression of remodeling may favor delayed healing, bone exposure, infection, and sequestration.

Dental implants represent a clinically relevant but incompletely understood factor in MRONJ. Implants may be present before antiresorptive therapy, inserted during or after therapy, or become involved secondarily when MRONJ progresses through peri-implant and alveolar bone [5,6]. For clinicians, the key question is not only whether implants survive, but whether the peri-implant interface remains biologically viable and mechanically reliable over time. This distinction is particularly important in medically compromised or oncologic patients, in whom a clinically stable implant may coexist with progressive osteonecrosis.

Dental implants represent a relevant clinical consideration in patients receiving antiresorptive therapy because of the potential risk of medication-related osteonecrosis of the jaw (MRONJ). Recent systematic evidence has evaluated both implant failure and MRONJ associated with dental implants in patients receiving antiresorptive therapy for osteoporosis. A 2025 systematic review and meta-analysis identified 186 cases of MRONJ among implant recipients and estimated a pooled MRONJ rate of approximately 0.5% following implant placement, while bisphosphonate exposure was associated with an increased risk of MRONJ [6]. Nevertheless, the available evidence remains heterogeneous and provides limited information regarding the biological characteristics of the bone–implant interface once MRONJ is established.

Most mechanistic evidence regarding MRONJ and implant-related osteonecrosis derives from animal models [7–9]. Although such models are valuable, their translation to human implant dentistry is limited by differences in bone remodeling, microbial exposure, prosthetic loading, drug protocols, and disease duration. Human implant-retrieval studies are therefore essential because they allow direct evaluation of the interface between implant surfaces and affected bone. However, human retrievals containing multiple osseointegrated implants within a MRONJ sequestrum are extremely uncommon.

Previous work using histology and synchrotron radiation-based microtomography has shown that human jawbone affected by antiresorptive-related osteonecrosis may exhibit regional heterogeneity in mineralization, trabecular morphology, osteocyte lacunar distribution, and resorption patterns [10–12]. These observations suggest that MRONJ lesions are structurally heterogeneous and that peri-implant bone exposed to mechanical loading may differ from inter-implant bone not directly contacting the implant surface. Advanced phase-contrast microtomography can complement undecalcified histology by enabling three-dimensional assessment of lacunar morphology, local mineralization, and microstructural damage at submicrometric resolution.

The aim of the present ex vivo human retrieval study was to characterize the bone–implant interface in an extensive denosumab-associated mandibular MRONJ sequestrum containing five Morse taper connection implants. The primary objective was to quantify persistent bone-to-implant contact within the MRONJ-affected interface using histomorphometry, without assuming that such contact represented biologically viable osseointegration. The secondary objectives were to compare peri-implant and inter-implant bone, evaluate osteonecrotic and resorption-related histological features, and assess osteocyte lacunar morphology and relative mineralization using synchrotron phase-contrast microtomography. The study was designed to address topics central to contemporary implantology, including the biology of osseointegration, implant complications in medically compromised patients, and the interpretation of implant survival versus success.

2. Materials and Methods

2.1. Study Design and Specimen Source

This investigation was designed as a single-patient, descriptive human retrieval case study with multimodal ex vivo analysis. The records of the Implant Retrieval Center, Department of Medical, Oral and Biotechnological Sciences, University of Chieti-Pescara, Italy, were reviewed to identify peri-implant bone specimens associated with an extensive MRONJ-related mandibular sequestrum containing dental implants that had been clinically stable before and during the development of MRONJ. The clinical history was used to contextualize the specimen and to identify relevant risk factors; for descriptive purposes, the retrieved implants, peri-implant bone regions, and inter-implant bone regions were treated as nested analytical units within a single-patient retrieval; they were not considered biologically independent replicates.

2.2. Clinical Context of the Retrieved Mandibular Segment

The specimen originated from a male patient in his late sixties at the beginning of the observation period. The patient had been rehabilitated since the late 1990s with a combined prosthesis consisting of anterior fixed elements supported by natural teeth and two implants in the left posterior mandible. The most distal implant showed chronically evolving but asymptomatic peri-implantitis that remained clinically stable for several years. Periodic non-surgical maintenance included Vector instrumentation and peri-implant laser therapy (Erbium Key laser, 80–120 mJ, 10–15 Hz; KaVo, Biberach, Germany). The patient reported heavy tobacco exposure, approximately 20 cigarettes per day for more than 50 years.

At T0, approximately 10 years after the initial prosthetic rehabilitation, panoramic radiography confirmed the stability of the implant-supported prosthesis (Figure 1a). The initial prosthetic rehabilitation was performed using the Ankylos system (Dentsply Sirona, Rome, Italy), originally placed at site #36, that was characterized by a self-locking conical connection, horizontal offset, progressive threading, a sandblasted surface, and a smooth collar.

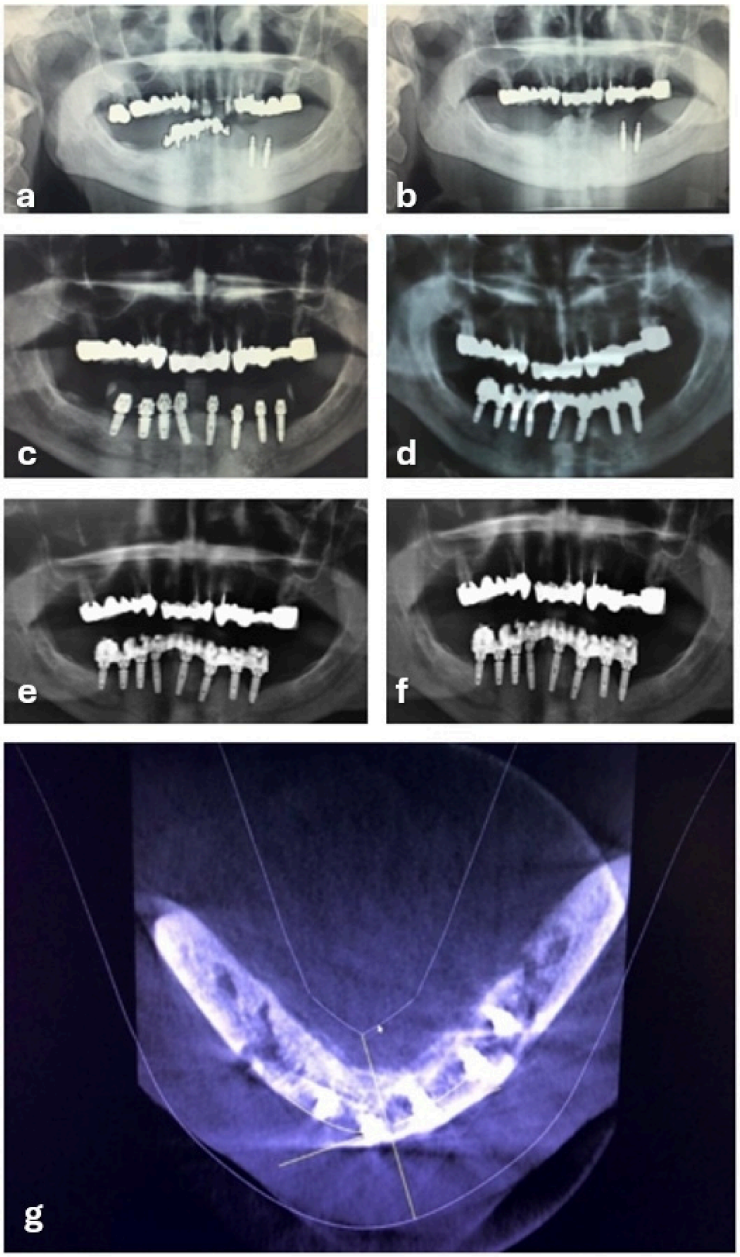

Figure 1. Radiographic imaging follow-up. (**a**) Panoramic radiograph at T0, approximately 10 years after initial prosthetic rehabilitation; (**b**,**c**) panoramic radiographs obtained between T0 + 5.5 and T0 + 6.5 years, documenting the initiation and completion of the surgical phase; (**d**) panoramic radiograph at T0 + 7 years, approximately 6 months after implant-prosthetic therapy; (**e**) panoramic radiograph at T0 + 7.1 years, showing an inflammatory process associated with a submental nodular mass; (**f**) panoramic radiograph at T0 + 7.7 years, showing bilateral mandibular osteonecrotic lesions; (**g**) CBCT reconstruction showing necrosis following an oblique vestibular-to-lingual and crestal-to-basal path, involving the implant fixtures within the necrotic bone.

At T0 + 5 years, failure of the anterior natural-tooth-supported prosthetic group led to full-arch fixed implant rehabilitation of the Toronto Bridge type. The surgical and prosthetic phases were completed between T0 + 5.5 and T0 + 6.5 years and initially showed uneventful clinical and radiographic outcomes (Figure 1b,c). In these prosthetic phases, implants (from 4 × 8 mm to 5 × 11 mm) manufactured by Implacil De Bortoli (São Paulo, Brazil) were placed, featuring a sandblasted and acid-etched surface, a conical (Cone Morse) connection, and a threaded implant body. The implants were placed at sites #47, #45, #31, and #33.

Medical history included radical prostatectomy for prostate adenocarcinoma approximately five years before T0. At T0 + 6.5 years, because of osseous recurrence, systemic oncologic therapy was initiated, including subcutaneous denosumab at 120 mg every 4 weeks (Xgeva). A follow-up radiograph at T0 + 7 years, approximately six months after completion of implant-prosthetic therapy, did not show complications (Figure 1d). At T0 + 7.1 years, diffuse dull pain developed in the left posterior mandible, followed by bilateral pain and migrating paraesthesia. Radiographic and computed tomographic imaging showed inflammatory changes and a firm submental nodular mass of approximately 2 cm (Figure 1e).

The lesion temporarily regressed after intramuscular ceftriaxone therapy but recurred after antibiotic discontinuation. At T0 + 7.2 years, denosumab therapy was suspended, and the patient was referred for dental evaluation. Serum CTX values remained markedly low, with the latest recorded value below 90 pg/mL. This finding was reported as part of the patient's biochemical assessment. Between T0 + 7.4 and T0 + 7.7 years, symptoms fluctuated despite repeated antibiotic and anti-inflammatory treatment. Cone beam computed tomography revealed a bilateral mandibular osteonecrotic lesion extending continuously from the right to the left molar region, with a demarcation between necrotic and viable bone. The lesion followed an oblique vestibular-to-lingual and crestal-to-basal course and included all implant fixtures within the necrotic bone, although the implants remained clinically stable (Figure 1f,g).

Between T0 + 8.1 and T0 + 8.5 years, gingival recession and exposure of necrotic bone developed. Conservative local management included chlorhexidine irrigation, topical rifamycin, metronidazole gel, saline irrigation, and atraumatic debridement with Teflon instruments. Specialist evaluation confirmed extensive osteolytic changes, cortical discontinuities, and exposed lingual alveolar bone. Around T0 + 9.2 years, mobility of the necrotic mandibular segment became evident and progressively caused functional discomfort. The segment was later spontaneously expelled as a complete anatomical specimen. The patient could not be followed further because of hospitalization for pulmonary complications and subsequently died from acute pneumonia.

At the clinically most advanced stage, the patient was considered to have disease consistent with Stage 3 MRONJ according to the 2022 AAOMS classification [1], based on the presence of exposed necrotic bone with pain and infection and extensive mandibular osteolysis extending beyond the alveolar bone.

The condensed clinical timeline contextualizing the retrieved MRONJ mandibular segment is reported in Table 1.

Table 1. Condensed clinical timeline.

Time Point	Main Clinical/Radiographic Event	Relevance to Retrieval Analysis
Late 1990s	Initial combined prosthetic rehabilitation with two posterior mandibular implants.	Long-standing pre-existing implant integration before denosumab therapy.
T0	Panoramic radiograph confirmed continued prosthetic stability.	Baseline clinical stability of implant-supported rehabilitation.

Table 1. *Cont.*

Time Point	Main Clinical/Radiographic Event	Relevance to Retrieval Analysis
T0 + 5 to T0 + 6.5 years	Full-arch fixed implant-supported rehabilitation completed after anterior prosthetic failure.	Additional implants placed and loaded before MRONJ onset.
T0 + 6.5 years	Osseous recurrence of prostate cancer; denosumab 120 mg every 4 weeks initiated.	Systemic antiresorptive exposure relevant to MRONJ pathogenesis.
T0 + 7.1 years	Mandibular pain, paraesthesia, inflammatory submental mass.	Early clinical manifestation of jaw complication.
T0 + 7.2 to T0 + 7.7 years	Denosumab suspended; CTX < 90 pg/mL; CBCT showed bilateral osteonecrotic lesion including implants.	Low CTX value documented during radiographic progression despite implant stability.
T0 + 8.1 to T0 + 8.5 years	Necrotic bone exposure and conservative local treatment.	Transition to exposed MRONJ with secondary contamination risk.
T0 + 9.2 years and later	Progressive mobility and spontaneous expulsion of a mandibular sequestrum containing five implants.	Specimen available for histological, histomorphometric, and synchrotron analyses.

2.3. Ethical Approval and Consent

The study was conducted in accordance with the Declaration of Helsinki and was approved by the Territorial Ethics Committee of the Abruzzo Region (C.E.t.R.A.; third amendment approval no. 22, 9 May 2024, BONEISTO study). The patient received comprehensive information regarding the study protocol and provided written informed consent for participation and publication of anonymized clinical data and images.

2.4. Macroscopic Sampling and Specimen Processing

The necrotic mandibular segment containing five dental implants (Figure 2a) was immediately fixed in 10% buffered formalin. The block was sectioned to separate the implant-containing regions and the edentulous bone portions located between implants, which were defined as inter-implant bone (Figure 2b). For anatomical identification, the sampled inter-implant bone regions were designated according to the adjacent implants: the AB zone corresponded to the bone between implants A and B, BC zone to the bone between implants B and C, and CD zone to the bone between implants C and D. All samples underwent histological analysis. In addition, selected peri-implant bone fragments removed from implant surfaces and inter-implant bone portions were submitted to synchrotron radiation-based phase-contrast microtomography. Sampling of peri-implant tissue for synchrotron analysis followed the protocol described by Iezzi et al. [13].

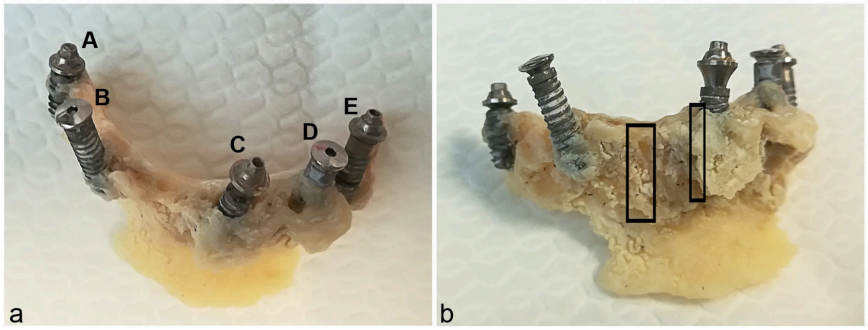

Figure 2. Macroscopic specimen and sampling strategy. (**a**) Necrotic mandibular segment containing five dental implants (A–E). (**b**) Examples of peri-implant and inter-implant bone portions submitted to synchrotron radiation imaging are highlighted.

2.5. Undecalcified Histology and Histomorphometry

The implants and inter-implant bone portions were processed for thin ground sections using an automated system (Precise 1, Assing, Rome, Italy). After fixation, specimens were dehydrated in a graded ethanol series and embedded in glycol-methacrylate resin (Technovit 7200 VLC, Kulzer, Wehrheim, Germany). After polymerization, specimens were sectioned in a buccal–lingual plane along the longitudinal axis with a high-precision diamond disc. Sections were initially cut to approximately 150 µm and then ground to a final thickness of approximately 80 µm using the Precise 1 automated system. Sections were stained with acid fuchsin and toluidine blue.

Histological evaluation was performed using transmitted light microscopy (Laborlux S, Leitz, Wetzlar, Germany) equipped with a high-resolution video camera (3CCD, model KY-F55B, JVC, Yokohama, Japan) connected to a computerized image analysis system. Histomorphometry was performed with a digitizing tablet (Matrix Vision GmbH, Oppenweiler, Germany) and Image-Pro Plus 4.5 software (Media Cybernetics Inc.; distributed by Immagini e Computer Snc, Milan, Italy). For histological classification, vital bone was operationally defined as mineralized bone showing preserved bone architecture and osteocyte-containing lacunae, with no evidence of widespread osteocyte lacunar emptiness or other morphological features of necrosis. Non-vital bone was defined as mineralized bone showing predominantly empty osteocyte lacunae and/or other morphological evidence of necrotic tissue, including microfractures and loss of normal tissue organization [10,12].

Bone-to-implant contact (BIC) was quantified in two ways. Endosseous BIC (EBIC) was calculated by considering the endosseous portion of the implant. First-point BIC (FBIC) was calculated from the first coronal bone-to-implant contact to the implant apex, thereby estimating the remaining contact independently of coronal crestal resorption. Histological variables included vital and non-vital bone, empty osteocyte lacunae, microfractures, bacterial colonies, demineralized bone, bone remodeling, Howship-like lacunae, osteoclasts, and osteoblastic activity.

2.6. Synchrotron Radiation-Based Phase-Contrast Microtomography

Microtomographic imaging was performed at the SYRMEP imaging beamline of the Elettra Synchrotron Facility, Basovizza, Trieste, Italy. For each sample, 1800 projections were acquired over 180° of rotation with an exposure time of 0.5 s per projection. A white beam filtered through a 1.5 mm silicon plate produced a peak energy of 21 keV. The sample-to-detector distance was 100 mm to enable phase-contrast imaging. Raw images were captured using an Orca Flash 4.0 CMOS camera (2048 × 2048 pixels; pixel size 6.5 × 6.5 µm) coupled with a 17 µm GGG scintillator. The optical magnification system provided an effective pixel size of 0.9 × 0.9 μm^2 and a field of view of 1.8 × 1.8 mm^2.

Datasets were reconstructed using SYRMEP Tomo Project 1.6.3 software (ELETTRA in-house software, Basovizza (TS), Italy) [14]. Reconstruction included Rivers ring removal (wd = 7), phase retrieval using the Paganin TIE-Hom algorithm [15], and filtered back projection with a Shepp–Logan filter. Phase retrieval used a fixed δ/β ratio of 100. In the X-ray regime, the complex refractive index is expressed as $n = 1 - \delta + i\,\beta$, where δ represents the phase shift and β is proportional to the absorption coefficient. The δ/β ratio was selected empirically to optimize bone tissue visualization. Each reconstructed dataset consisted of 2048 slices and was converted to 8-bit images by remapping the original 32-bit data within the real-value range 0.0002–0.0008.

Image processing and analysis were performed using Dragonfly software (Dragonfly 2022.2, Comet Technologies Canada Inc., Montreal, QC, Canada) [16]. A pretrained U-Net model available in Dragonfly was used for the automated segmentation of osteocyte lacu-

nae [17]. From each sample, two sequential 1 mm^3 sub-volumes were virtually extracted. Segmentation output was visually reviewed in each sub-volume to identify obvious misclassifications of lacunae, vascular spaces, microcracks, and imaging artefacts. No formal quantitative validation against an independently annotated ground-truth dataset was performed in the present MRONJ samples. Therefore, segmentation accuracy was assessed qualitatively by expert visual review, and the possibility of residual misclassification cannot be excluded.

2.7. Osteocyte Lacunae Shape Complexity Features

Only segmented structures with volumes between 80 and 980 μm^3 were included as morphometrically compatible with osteocyte lacunae. The lower threshold was selected to exclude voids too small to plausibly accommodate an osteocyte, whereas the upper threshold was intended to exclude spaces excessively large to represent individual osteocyte lacunae and more likely attributable to vascular spaces, microcracks, or segmentation artefacts. This range was adopted from our previous synchrotron-based morphometric study [17], performed using the same experimental setup, effective pixel size, peak energy, and segmentation workflow.

The following parameters were assessed: average lacuna volume (LacVol, μm^3); mean lacuna volume-to-surface ratio (LacV/S, μm); three-dimensional lacunar aspect ratio (LacAR), defined as the ratio between the shortest and longest lacunar axes; lacunar sphericity (LacS), defined by comparison of the surface area of a sphere of equivalent volume with the actual lacunar surface area; and specific lacunar numerical density (LacNr, mm^{-3}), defined as the number of lacunae per cubic millimeter of bone matrix. Because the analyzed sub-volumes were similar but not perfectly identical in volume, LacNr was used as the volume-normalized descriptor of lacunar abundance, rather than absolute lacunar counts, for comparisons among anatomical regions.

2.8. Relative Bone Mineralization Distribution

Starting from the reconstructed complex refractive index, which is linearly related to mass density, apparent relative bone mineralization distribution (BMD_r) was assessed in the regions of interest according to Roschger et al. [18]. BMD_r parameters were computed within the mineralized matrix. Because the analysis used a fixed δ/β ratio and a polychromatic white X-ray beam, absolute calcium content could not be directly measured. Therefore, all mineralization parameters are reported as relative($_r$) values. Pixel intensity frequency distributions from 0 to 255 on the 8-bit scale were used to compare mean opacity values between samples. Because the regions of interest were comparable in size and composition, relative differences in mineralization distribution were considered suitable for comparative interpretation. The mean relative mass density (BMD_r-mean) and full width at half maximum of the mineralization distribution (BMD_r-FWHM) were extracted using PeakFit v4.12 software (Systat Software, San Jose, CA, USA).

2.9. Statistical Analysis

Quantitative data are reported as mean ± standard deviation (SD). The analysis of phase-contrast microtomography data was performed using GraphPad Prism, version 10.0.0 (GraphPad Software, Boston, MA, USA). Because all specimens originated from a single patient and multiple lacunae were nested within a limited number of anatomical samples and sub-volumes, all analyses were considered exploratory. Spearman rank correlation coefficients were calculated to describe associations among osteocyte lacunar morphometric features. Correlation strength was classified as very weak (ρ = 0.00–0.20), weak (ρ = 0.21–0.40), moderate (ρ = 0.41–0.60), strong (ρ = 0.61–0.80), or very strong (ρ = 0.81–1.00). The analyses did not account for biological clustering; therefore, *p*-values

should be interpreted cautiously and no population-level inference was intended. EBIC and FBIC values were summarized descriptively because they were paired, mathematically related measurements obtained from five implants within the same patient.

3. Results

3.1. Macroscopic and Histological Overview of the Bone–Implant Interface

At low magnification, all five implants showed persistent areas of direct bone-to-implant contact despite their inclusion within the necrotic mandibular sequestrum (Figure 3). The surrounding bone was predominantly mature compact mandibular bone with small marrow spaces. Bone loss was concentrated in the buccal and coronal regions. Implants A and D maintained bone in the coronal portion, whereas implant C showed marked bone loss with a saucer-shaped buccal depression. No microgap between implant and abutment was observed in any analyzed section.

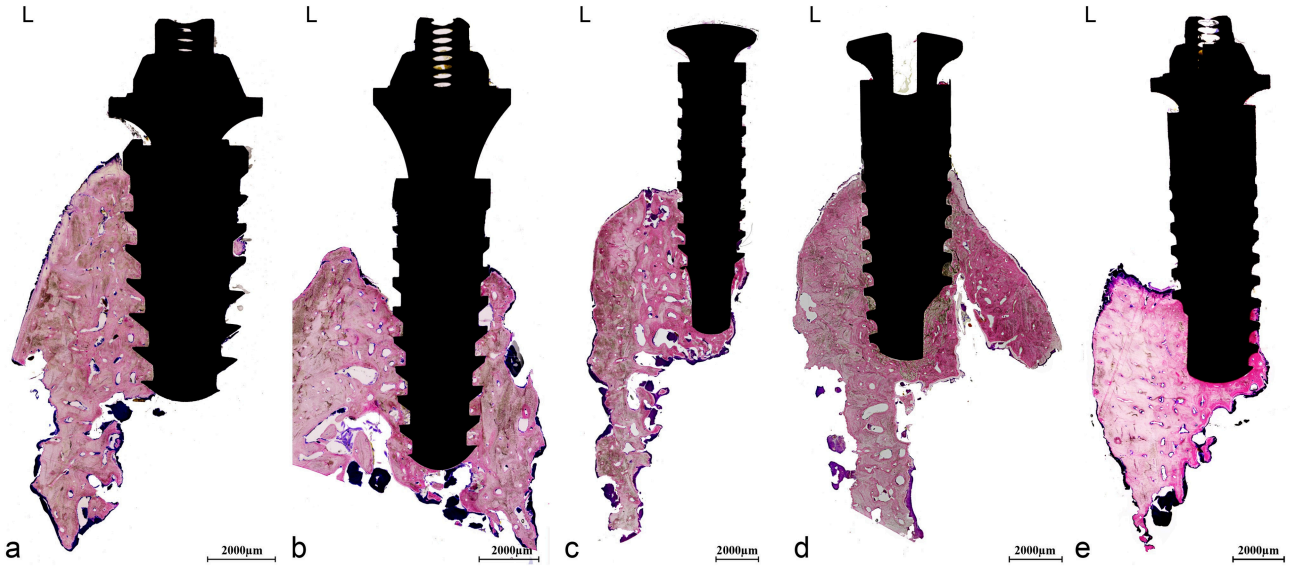

Figure 3. Buccal–lingual histological sections of implants A–E. L indicates the lingual side. No microgap between implant and abutment was observed. (**a**) Compact bone with small marrow spaces contacted the implant surface only on the lingual side. (**b**) Crestal bone resorption was present at lingual and buccal sites; compact bone with remodeling was observed apically. (**c**) Coronal bone resorption with saucer-shaped buccal depression. (**d**) Implant surrounded by compact bone. (**e**) Apical implant portion surrounded by compact bone with very small marrow spaces. Original magnification 100×; acid fuchsin–toluidine blue.

At higher magnification, multiple areas of bone remodeling were present around the implants, although reversal lines were poorly defined (Figure 4). Areas classified as non-vital bone according to the predefined histological criteria showed predominantly empty osteocyte lacunae and were frequently associated with microfractures and bacterial colonies. In contrast, areas classified as vital bone retained osteocyte-containing lacunae and preserved mineralized bone architecture. Residual areas of vital bone contacting the implant surface were also observed. Lamellar bone contained few osteocyte lacunae, many of which were empty. Variable amounts of necrotic and completely demineralized bone were present in direct contact with the implant surface.

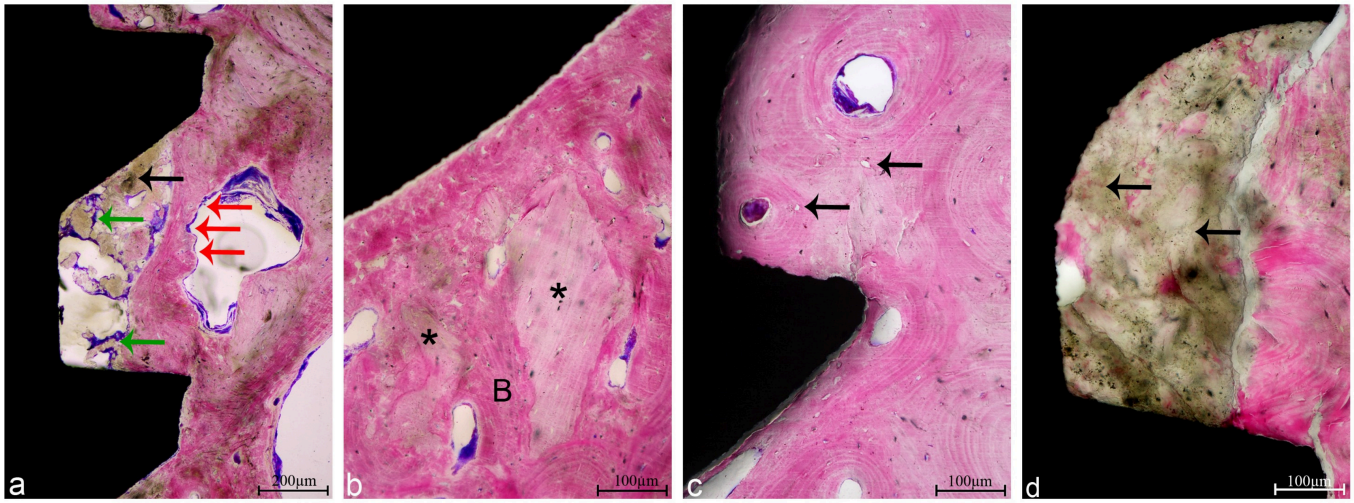

Figure 4. Higher-magnification histology of peri-implant bone. (**a**) Non-viable bone (black arrows) associated with bacterial colonies (green arrows) within implant threads; Howship-like lacunae (red arrows) were also detected. (**b**) Non-vital bone (*) surrounded by vital bone (B) in the apical portion. (**c**) Lamellar bone with few osteocyte lacunae, many empty (black arrows). (**d**) Demineralized bone (black arrows) inside an implant concavity. Original magnification 100×–200×; acid fuchsin-toluidine blue.

The presence of Howship-like resorption lacunae in the absence of identifiable osteoclasts is compatible with prior resorptive activity, although the timing and cellular mechanism cannot be established from static histology (Figure 5a). No osteoblastic activity was observed in the examined fields. Inter-implant bone showed some features similar to peri-implant bone, including areas with empty osteocyte lacunae alternating with vital bone (Figure 5b,c). However, inter-implant bone showed fewer alterations than peri-implant bone: microfractures, necrotic bone directly contacting implant surfaces, complete demineralization, and heavy bacterial colonization were less evident or absent.

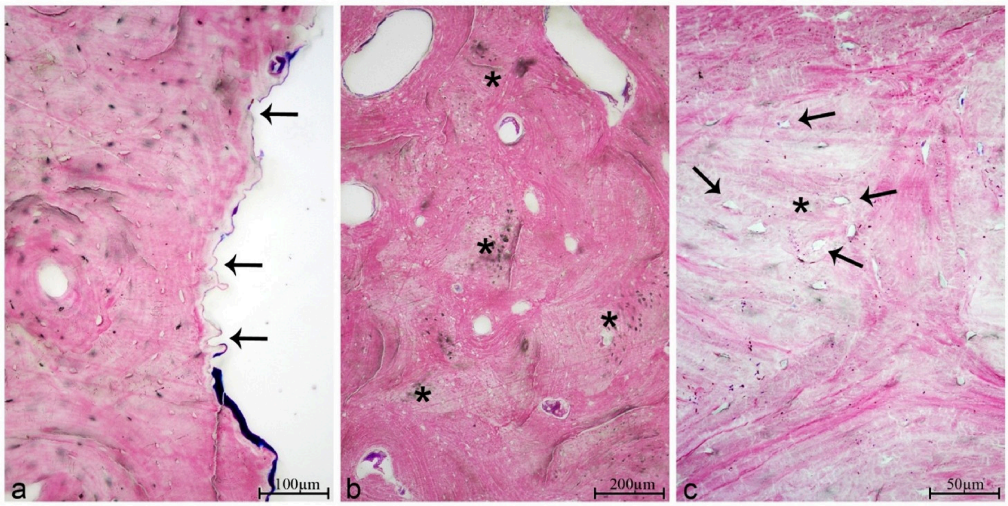

Figure 5. Histology of resorption of inter-implant bone regions. (**a**) Numerous Howship-like lacunae (black arrows) were present, although osteoclasts were not detected. (**b**) In inter-implant bone, vital bone surrounded non-vital areas (*). (**c**) Non-vital bone (*) with empty osteocyte lacunae (black arrows). Original magnification 100×–400×; acid fuchsin-toluidine blue.

3.2. Histomorphometric Bone-to-Implant Contact

Histomorphometry confirmed persistent bone-to-implant contact around all five implants (Table 2). Mean EBIC was 42.45 ± 13.41%, whereas mean FBIC was 84.40 ± 4.17%.

Given the single-patient design and the mathematical dependence between the two BIC measures, the comparison was interpreted descriptively rather than inferentially. This discrepancy indicates that extensive crestal and buccal bone loss reduced total endosseous contact, whereas substantial contact persisted below the first coronal bone-contact point.

Table 2. Bone-to-implant contact for implants A-E, calculated as endosseous BIC (EBIC) and first-point BIC (FBIC).

Implant	EBIC (%)	FBIC (%)
A	37.85	91.16
B	32.32	82.97
C	54.91	84.52
D	58.38	83.51
E	28.81	79.85
Mean ± SD	42.45 ± 13.41	84.40 ± 4.17

3.3. Phase-Contrast Microtomography

Three-dimensional phase-contrast microtomography confirmed pronounced resorption-related surface irregularities throughout the examined osteonecrotic mandibular tissue. Two-dimensional (Figure 6a) and three-dimensional reconstructions (Figure 6b) showed indented bone surfaces morphologically compatible with previous resorptive activity, consistent with the histological observation of Howship-like lacunae. Segmented osteocyte lacunae showed descriptively lower values in effective lacunar size and numerical density than those reported in previously published non-pathological peri-implant and regenerative datasets (Figure 6c) [17,19]. Both historical reference datasets [17,19] were acquired using the same synchrotron experimental setup, including the same effective pixel size and peak energy, and were analyzed using comparable reconstruction and segmentation procedures, supporting their use for descriptive contextualization.

Quantitative analysis of osteocyte lacunar shape complexity features (Table 3) showed a lower mean lacunar volume and lower lacunar numerical density in the MRONJ peri-implant samples than in reference non-pathological and regenerative conditions. Within the MRONJ specimen, inter-implant bone showed a less pronounced reduction in lacunar volume and density than peri-implant bone. These findings are consistent with the histological observation that peri-implant regions exhibited greater structural injury than inter-implant regions.

Table 3. Osteocyte lacunae network shape complexity features in peri-implant and inter-implant bone regions. Data are reported as mean ± SD. Historical reference values derived from previously published datasets.

Parameter	Peri-Implant	Ctr*	AB Zone	BC Zone	CD Zone	Ctr** Regeneration
LacVol (μm^3)	256 ± 47	481 ± 55	292 ± 28	291 ± 43	215 ± 29	426 ± 42
LacV/S (µm)	1.05 ± 0.08	-	1.02 ± 0.03	1.11 ± 0.06	1.02 ± 0.04	1.24 ± 0.05
LacAR	0.416 ± 0.018	0.392 ± 0.025	0.325 ± 0.039	0.348 ± 0.013	0.371 ± 0.015	0.334 ± 0.019
LacS	0.839 ± 0.029	0.855 ± 0.011	0.830 ± 0.008	0.842 ± 0.002	0.853 ± 0.003	0.825 ± 0.013
LacNr (mm^{-3}) × 10^4	0.87 ± 0.48	2.73 ± 0.27	1.32 ± 0.20	1.42 ± 0.32	1.01 ± 0.22	1.82 ± 0.32

AB zone: bone between implants A and B; BC zone: bone between implants B and C; and CD zone: bone between implants C and D. Ctr* refers to the non-pathological control dataset reported by Riberti [19]. Ctr** regeneration refers to the regenerative dataset reported by Mangano et al. [17]. Both historical reference datasets were obtained using the same synchrotron experimental setup and the same reconstruction and segmentation procedures.

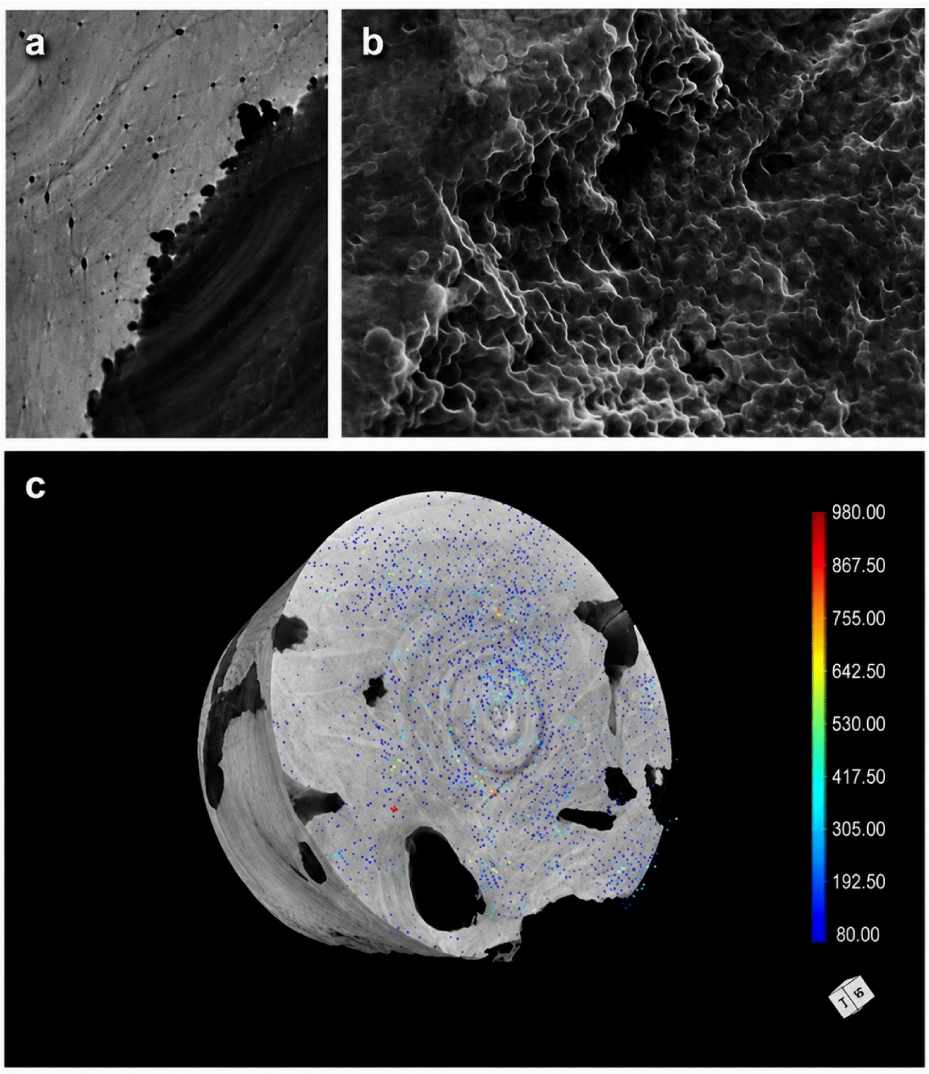

Figure 6. Phase-contrast microtomography analysis. (**a**) Two-dimensional detail showing surface irregularities morphologically compatible with resorption. (**b**) Three-dimensional surface detail further illustrating resorption-related irregularities. (**c**) Representative sub-volume with osteocyte lacunae segmented by neural network; color coding represents lacunar volume distribution (μm^3).

Relative bone mineralization (BMD_r) analysis demonstrated heterogeneity of mineralization distribution within the examined mandibular segment (Table 4). This phenomenon was most evident in peri-implant regions, where broader BMD_r-FWHM values indicated a wider distribution of mineralization levels than that in bone regions farther from the implant.

Table 4. Relative bone mineralization distribution in the patient biopsy. AB zone: bone between implants A and B; BC zone: bone between implants B and C; and CD zone: bone between implants C and D.

	Region	BMDr-Mean (Relative Gray Value)	BMDr-FWHM (Relative Gray Value)	Interpretation
Peri-implant bone	-	156 ± 12	50 ± 9	broad distribution
Inter-implant bone	AB zone	181 ± 15	39 ± 3	narrower distribution than peri-implant bone
	BC zone	147 ± 3	22 ± 2	
	CD zone	195 ± 5	29 ± 5	

Spearman rank correlation analysis (Table 5) showed a very strong positive association between lacunar numerical density and LacV/S ($\rho = 0.85$, $p < 0.0001$), and a strong positive association between lacunar numerical density and LacVol ($\rho = 0.80$, $p < 0.0001$). LacNr was strongly negatively correlated with LacAR ($\rho = -0.67$, $p = 0.0007$), suggesting that regions with more numerous effective lacunae tended to contain larger, less elongated lacunae. LacS was not significantly correlated with LacNr.

Table 5. Spearman rank correlation analysis between osteocyte lacunar network structural indices. Exact *p*-values are reported for descriptive purposes only. Because the observations are non-independent and the analyses did not account for biological clustering, *p*-values should be interpreted cautiously and no confirmatory or population-level inference is intended.

Variable	LacNr	LacVol	LacV/S	LacAR	LacS
LacNr	$\rho = 1$	$\rho = 0.80$; $p < 0.0001$	$\rho = 0.85$; $p < 0.0001$	$\rho = -0.67$; $p = 0.0007$	$\rho = -0.22$; $p = 0.321$
LacVol	-	$\rho = 1$	$\rho = 0.96$; $p < 0.0001$	$\rho = -0.39$; $p = 0.0708$	$\rho = -0.42$; $p = 0.051$
LacV/S	-	-	$\rho = 1$	$\rho = -0.45$; $p = 0.0371$	$\rho = -0.29$; $p = 0.197$
LacAR	-	-	-	$\rho = 1$	$\rho = 0.48$; $p = 0.024$
LacS	-	-	-	-	$\rho = 1$

4. Discussion

This multimodal human retrieval case study provides direct evidence that substantial bone-to-implant contact can persist within an extensive denosumab-associated mandibular MRONJ sequestrum despite severe loss of biological integrity of the surrounding bone. Importantly, the persistence of histomorphometric contact should not be interpreted as evidence of viable osseointegration. The principal findings were as follows: first, all five implants retained persistent bone-to-implant contact despite being included in necrotic bone; second, EBIC was markedly lower than FBIC, indicating that coronal and buccal resorption reduced total endosseous contact while substantial bone contact persisted along apical and residual portions of the implant surface; third, peri-implant bone showed greater microstructural damage than inter-implant bone; and fourth, synchrotron phase-contrast microtomography confirmed alterations in osteocyte lacunar morphology and mineralization heterogeneity that are not fully appreciable by conventional two-dimensional histology alone.

The distinction between implant stability relative to the surrounding bone and mobility of the entire necrotic segment is central to the interpretation of this case. During the earlier phases of MRONJ progression, the implants remained clinically stable relative to the surrounding mandibular bone despite severe biological deterioration of the peri-implant interface. Histologically, substantial bone-to-implant contact persisted, particularly below the first coronal bone-contact point. However, this contact involved bone showing necrosis, empty osteocyte lacunae, bacterial colonization, microfractures, and impaired remodeling. At a later stage, the necrotic mandibular segment itself became mobile, and the implants contained within it consequently moved together with the sequestrum rather than becoming individually mobile relative to the surrounding bone. Therefore, the absence of individual implant mobility should not be regarded as evidence of biological integrity of the peri-implant interface or long-term implant success in MRONJ.

The observed EBIC of $42.45 \pm 13.41\%$ reflected the loss of coronal and buccal bone. In contrast, the FBIC of $84.40 \pm 4.17\%$ showed that the remaining endosseous interface below the first contact point was still largely mineralized and attached to implant surfaces. This pattern suggests that MRONJ-associated bone loss may progress regionally rather than through uniform detachment of the implant surface. For clinicians, such a pattern may

explain why implants can remain stable relative to the surrounding bone during earlier phases of MRONJ progression, despite radiographic evidence of advancing osteonecrosis.

The peri-implant region showed more severe structural alterations than inter-implant bone, including microfractures, demineralized bone at the implant surface, and greater bacterial colonization. Functional loading normally stimulates peri-implant remodeling and adaptation; however, in the context of antiresorptive therapy and suppressed bone turnover, the capacity to repair microdamage may be reduced. The absence of osteoblastic activity and the presence of Howship-like lacunae without active osteoclasts support the interpretation of disrupted remodeling dynamics. This finding agrees with previous human observations of vital and non-vital bone juxtaposed at implant surfaces affected by osteonecrosis [20,21] and with histological evidence that peri-implant bone differs from inter-implant bone [22,23].

The patient also had major co-factors relevant to complications and long-term implant outcomes, including metastatic cancer, high-dose oncologic denosumab, heavy smoking, previous peri-implantitis at one implant site, repeated inflammatory episodes, and prolonged antibiotic and local conservative treatment. The present study cannot isolate the causal contribution of each factor. Nevertheless, systemic suppression of bone turnover and local peri-implant challenge may represent biologically plausible contributors to the severity of the observed interface damage [24,25].

Synchrotron phase-contrast microtomography showed reduced effective osteocyte lacunar volume and density, particularly in peri-implant bone. Osteocytes are essential regulators of bone mechanosensation, mineral homeostasis, and remodeling. A reduced population of effective lacunae, together with empty lacunae observed histologically, indicates compromised cellular viability and impaired capacity for adaptive response. The strong correlations between lacunar density, lacunar volume, and LacV/S suggest that regions containing more numerous effective lacunae also retained larger and potentially more functional osteocyte spaces.

Relative bone mineralization was heterogeneous, especially near implants. Mineralization heterogeneity may alter local mechanical properties [26,27], promoting stress concentration and microdamage accumulation. In the setting of MRONJ, this may contribute to a cycle in which impaired remodeling prevents repair of microcracks, bacterial contamination maintains inflammation, and progressive sequestration undermines the bone–implant interface. These microstructural findings expand earlier observations on MRONJ bone heterogeneity obtained through histology and synchrotron microtomography [10,12].

Two implants retained coronal bone despite the surrounding osteonecrotic process, and no implant–abutment microgap was observed histologically in any analyzed section. These findings are compatible with the possibility that Morse taper conical connections may reduce bacterial penetration or micromovement at the implant–abutment interface [28,29]. However, the present study does not provide evidence of superiority of a specific implant design because there was no control implant system, no randomized comparison, and no pre-MRONJ histological baseline. The observation should therefore be interpreted as hypothesis-generating. Future retrieval studies and controlled clinical cohorts are needed to determine whether conical connections influence peri-implant bone preservation in patients receiving antiresorptive drugs.

This study has direct implications for clinical effectiveness, complications, long-term results, implant success, and survival. In patients receiving high-dose antiresorptive therapy, implant stability alone may be insufficient for defining success [24,30,31]. Long-term assessment should integrate systemic risk, drug type and dose, cancer status, smoking, peri-implant inflammation, mucosal health, radiographic bone changes, and signs of MRONJ.

When implants are already present before oncologic denosumab therapy, multidisciplinary communication between oncologists, oral surgeons, periodontists, prosthodontists, and implant clinicians is critical. Preventive maintenance should focus on reducing peri-implant inflammation, avoiding traumatic procedures when possible, and promptly investigating pain, paraesthesia, exposed bone, or unexplained inflammatory masses [32,33].

The findings do not imply that implants should be routinely removed in patients receiving antiresorptive therapy. Rather, they emphasize that the biological condition of peri-implant bone may deteriorate even when individual implant mobility relative to the surrounding bone is absent. The results support a risk-based, patient-centered approach in which implant survival is assessed alongside clinical, radiographic, and biological indicators of peri-implant complications, as well as patient-specific systemic risk factors [34,35].

The main strength of this multimodal human retrieval case study is the rare availability of a human mandibular MRONJ sequestrum containing five implants, allowing direct histological and three-dimensional microstructural analysis of the bone–implant interface. The combination of undecalcified histology, histomorphometry, and synchrotron phase-contrast microtomography provides complementary information on tissue viability, bone contact, osteocyte lacunae, resorption morphology, and mineralization heterogeneity.

The study has several important limitations that should be considered when interpreting the findings. It was based on a single-patient retrieval and lacked a matched healthy intra-patient control. The five implants were anatomically clustered within the same patient and should therefore not be interpreted as independent biological replicates. The peri-implant and inter-implant regions were not matched for anatomical position, microbial exposure, local geometry, or mechanical strain; consequently, the observed regional differences cannot be attributed specifically to functional loading. The clinical course was also influenced by multiple potential confounders, including malignancy, high-dose denosumab exposure, heavy smoking, pre-existing peri-implantitis, local infection, and prolonged conservative treatment. In addition, spontaneous exfoliation of the sequestrum may have introduced post-necrotic mechanical damage. Histological baseline data obtained before the onset of MRONJ were unavailable. Absolute bone mineral density could not be quantified because the phase-retrieval method and polychromatic white-beam configuration allowed only relative assessment of bone mineralization distribution. Finally, the neural-network-assisted segmentation was not formally validated against an independently annotated ground-truth dataset in the present MRONJ samples; thus, segmentation-related measurement error and residual misclassification cannot be excluded.

Future research should establish multicenter human retrieval registries for implants affected by MRONJ, standardize histomorphometric definitions of persistent bone-to-implant contact in MRONJ-affected bone, and integrate microCT, synchrotron imaging, histology, microbiology, and clinical endpoints. Prospective studies in patients receiving antiresorptive therapy should distinguish implant survival from implant success and include long-term evaluation of complications [36,37]. The use of artificial intelligence for lacunar-network segmentation, combined with advanced imaging of the peri-implant interface, may provide quantitative structural descriptors of tissue deterioration in future validated studies [38–40].

5. Conclusions

Within the limitations of a single-patient human retrieval study, advanced denosumab-associated MRONJ can coexist with substantial persistent bone-to-implant contact around clinically stable dental implants. EBIC was reduced by extensive coronal and buccal bone loss, whereas FBIC showed substantial contact below the first point of bone attachment.

Importantly, such histomorphometric contact should not be equated with biologically viable osseointegration, as the peri-implant bone exhibited non-vital tissue, microfractures, bacterial colonization, empty osteocyte lacunae, demineralized areas, reduced lacunar density, and heterogeneous relative mineralization. This retrieval observation therefore highlights a dissociation between implant stability, persistent physical bone contact, and biological integrity of the bone–implant interface in MRONJ.

Author Contributions: Conceptualization, G.V., A.P., A.G. and G.I.; methodology, G.V., A.G., M.F., G.R., G.I., N.R. and M.P.; software, A.G., M.F., G.I., N.R., M.P. and T.V.P.; validation, G.V., A.G., G.R., A.P. and G.I.; formal analysis, A.G., M.F., A.P., G.I., N.R., M.P. and T.V.P.; investigation, G.V., A.G., M.F., G.R., A.P., G.I. and N.R.; resources, G.V., A.G., G.R., A.P. and G.I.; data curation, A.G., M.F., G.I. and N.R.; writing—original draft preparation, A.G., M.F., G.R., G.I., N.R., M.P. and T.V.P.; writing—review and editing, A.G., M.F., A.P., G.I., N.R., M.P. and T.V.P.; visualization, G.V., A.G., M.F., G.R., A.P., G.I., N.R., M.P. and T.V.P.; supervision, G.V., A.G., G.R., A.P., G.I. and M.P.; project administration, G.V., A.G., G.R., A.P., G.I., M.P. and T.V.P.; funding acquisition, G.V., G.R. and A.P. All authors have read and agreed to the published version of the manuscript.

Funding: This research received no external funding.

Institutional Review Board Statement: The study was conducted in accordance with the Declaration of Helsinki and approved by the Territorial Ethics Committee of the Abruzzo Region (C.E.t.R.A.; third amendment approval no. 22, 9 May 2024, BONEISTO study).

Informed Consent Statement: Written informed consent was obtained from the patient for participation in the study and for publication of anonymized clinical information and images.

Data Availability Statement: The data supporting the findings of this study are available from the corresponding author upon reasonable request. The data are not publicly available because of privacy and ethical restrictions.

Acknowledgments: We acknowledge Elettra Synchrotron Trieste for providing access to its synchrotron radiation facilities, and Giuliana Tromba for assistance in using beamline SYRMEP. The 3D reconstructions presented in this paper were generated using Dragonfly software, version 2022.2 for Windows (Object Research Systems [ORS] Inc., Montreal, Quebec, Canada; https://dragonfly.comet.tech/, accessed on 28 September 2026).

Conflicts of Interest: The authors declare no conflicts of interest.

Abbreviations

The following abbreviations are used in this manuscript:

MRONJ	medication-related osteonecrosis of the jaw
EBIC	Endosseous bone-to-implant contact
FBIC	first-point bone-to-implant contact
RANKL	receptor activator of nuclear factor-kappa B ligand
TIE	Transport of Intensity Equation
LacVol	average lacuna volume
LacV/S	mean lacuna volume-to-surface ratio
LacAR	three-dimensional lacunar aspect ratio
LacS	lacunar sphericity
LacNr	specific lacunar numerical density
BMDr-mean	mean relative mass density
BMDr-FWHM	full width at half maximum of the mineralization distribution

References

1. Ruggiero, S.L.; Dodson, T.B.; Aghaloo, T.; Carlson, E.R.; Ward, B.B.; Kademani, D. American Association of Oral and Maxillofacial Surgeons' Position Paper on Medication-Related Osteonecrosis of the Jaws-2022 Update. *J. Oral Maxillofac. Surg.* **2022**, *80*, 920–943. [CrossRef] [PubMed]
2. Yang, G.; Williams, R.; Wang, L.; Farhadfar, N.; Chen, Y.; Loiacono, A.T.; Bian, J.; Holliday, L.S.; Katz, J.; Gong, Y. Medication-related osteonecrosis of the jaw in cancer patients: Result from the OneFlorida Clinical Research Consortium. *J. Bone Miner. Res.* **2020**, *37*, 2466–2471. [CrossRef] [PubMed]
3. De Cicco, D.; Boschetti, C.E.; Santagata, M.; Colella, G.; Stagliano, S.; Gaggl, A.; Bottini, G.B.; Vitagliano, R.; D'amato, S. Medication-related osteonecrosis of the jaws: A comparison of SICMF-SIPMO and AAOMS guidelines. *Diagnostics* **2023**, *13*, 2137. [CrossRef] [PubMed]
4. Limones, A.; Saez-Alcaide, L.M.; Diaz-Parreno, S.A.; Helm, A.; Bornstein, M.M.; Molinero-Mourelle, P. Medication-related osteonecrosis of the jaws (MRONJ) in cancer patients treated with denosumab vs. zoledronic acid: A systematic review and meta-analysis. *Med. Oral Patol. Oral Cir. Bucal* **2020**, *25*, e326–e336. [CrossRef] [PubMed]
5. Pichardo, S.E.C.; van der Hee, J.G.; Fiocco, M.; Appelman-Dijkstra, N.M.; van Merkesteyn, J.P.R. Dental implants as risk factors for patients with medication-related osteonecrosis of the jaws (MRONJ). *Br. J. Oral Maxillofac. Surg.* **2020**, *58*, 771–776. [CrossRef] [PubMed]
6. Mirza, R.; El Rabbany, M.; Ali, D.S.; Tetradis, S.; Morrison, A.; Ruggiero, S.; Alnajimi, R.; Khan, A.A.; Guyatt, G. Dental implant failure and medication-related osteonecrosis of the jaw related to dental implants in patients taking antiresorptive therapy for osteoporosis: A systematic review and meta-analysis. *Endocr. Pract.* **2025**, *31*, 1189–1196. [CrossRef] [PubMed]
7. Zhu, W.Y.; Guo, J.; Yang, W.F.; Tao, Z.Y.; Lan, X.; Wang, L.; Xu, J.; Qin, L.; Su, Y.-X. Biodegradable magnesium implant enhances angiogenesis and alleviates medication-related osteonecrosis of the jaw in rats. *J. Orthop. Transl.* **2022**, *33*, 153–161. [CrossRef] [PubMed]
8. Bujila, A.; Silva, D.N.A.; Monajemzadeh, S.; da Silveira, T.M.; Elzakra, N.; Casarin, M.; Flores, K.; Magyar, C.; Marchesan, J.; Kim, R.; et al. Peri-implant inflammation increases the risk of osteonecrosis in mice treated with bisphosphonate. *J. Periodontol.* **2025**, *96*, 894–905. [CrossRef] [PubMed]
9. Quintao Manhanini Souza, E.; Felipe Toro, L.; Franzao Ganzaroli, V.; de Oliveira Alvarenga Freire, J.; Matsumoto, M.A.; Casatti, C.A.; Cintra, L.T.Â.; Buchaim, R.L.; Issa, J.P.M.; Garcia, V.G.; et al. Peri-implantitis increases the risk of medication-related osteonecrosis of the jaws associated with osseointegrated implants in rats treated with zoledronate. *Sci. Rep.* **2024**, *14*, 627. [CrossRef] [PubMed]
10. Giuliani, A.; Iezzi, G.; Mozzati, M.; Gallesio, G.; Mazzoni, S.; Tromba, G.; Cintra, L.T.Â.; Buchaim, R.L.; Issa, J.P.M.; Garcia, V.G.; et al. Bisphosphonate-related osteonecrosis of the human jaw: A combined 3D assessment of bone descriptors by histology and synchrotron radiation-based microtomography. *Oral Oncol.* **2018**, *82*, 200–202. [CrossRef] [PubMed]
11. Reznikov, N.; Bilton, M.; Lari, L.; Stevens, M.M.; Kroger, R. Fractal-like hierarchical organization of bone begins at the nanoscale. *Science* **2018**, *360*, eaao2189. [CrossRef] [PubMed]
12. Giuliani, A.; Iezzi, G.; Mozzati, M.; Gallesio, G.; Mazzoni, S.; Tromba, G.; Zanini, F.; Piattelli, A.; Mortellaro, C. Three-dimensional microarchitecture and local mineralization of human jaws affected by bisphosphonate-related osteonecrosis. *Oral Oncol.* **2018**, *84*, 128–130. [CrossRef] [PubMed]
13. Iezzi, G.; Di Lillo, F.; Furlani, M.; Degidi, M.; Piattelli, A.; Giuliani, A. The symmetric 3D organization of connective tissue around implant abutment: A key issue to prevent bone resorption. *Symmetry* **2021**, *13*, 1126. [CrossRef]
14. Brun, F.; Massimi, L.; Fratini, M.; Dreossi, D.; Bille, F.; Accardo, A.; Pugliese, R.; Cedola, A. SYRMEP Tomo Project: A graphical user interface for customizing CT reconstruction workflows. *Adv. Struct. Chem. Imaging* **2017**, *3*, 4. [CrossRef] [PubMed]
15. Paganin, D.; Mayo, S.C.; Gureyev, T.E.; Miller, P.R.; Wilkins, S.W. Simultaneous phase and amplitude extraction from a single defocused image of a homogeneous object. *J. Microsc.* **2002**, *206*, 33–40. [CrossRef] [PubMed]
16. Makovetsky, R.; Piche, N.; Marsh, M. Dragonfly as a platform for easy image-based deep learning applications. *Microsc. Microanal.* **2018**, *24*, 532–533. [CrossRef]
17. Mangano, C.; Riberti, N.; Orilisi, G.; Tecco, S.; Furlani, M.; Giommi, C.; Mengucci, P.; Giorgini, E.; Giuliani, A. Morphometric, biomechanical and macromolecular performances of beta-TCP macro/micro-porous lattice scaffolds fabricated via lithography-based ceramic manufacturing for jawbone engineering. *J. Funct. Biomater.* **2025**, *16*, 237. [CrossRef] [PubMed]
18. Roschger, P.; Paschalis, E.P.; Fratzl, P.; Klaushofer, K. Bone mineralization density distribution in health and disease. *Bone* **2008**, *42*, 456–466. [CrossRef] [PubMed]
19. Riberti, N.; D'Amico, E.; Cinquini, C.; Furlani, M.; Pierfelice, T.V.; Iezzi, G.; Longo, E.; Covelli, M.; Barone, A.; Giuliani, A. Retrospective clinical artificial intelligence-assisted study of loaded peri-implant versus edentulous bone. *Sci. Rep.* **2026**, *in press*. [CrossRef]
20. Favia, G.; Piattelli, A.; Sportelli, P.; Capodiferro, S.; Iezzi, G. Osteonecrosis of the posterior mandible after implant insertion: A clinical and histological case report. *Clin. Implant Dent. Relat. Res.* **2011**, *13*, 58–63. [CrossRef] [PubMed]

21. Ha, J.; Eo, M.Y.; Sodnom-Ish, B.; Mustakim, K.R.; Myoung, H.; Kim, S.M. Electron microscopic analysis of necrotic bone and failed implant surface in a patient with medication-related osteonecrosis of the jaw. *Maxillofac. Plast. Reconstr. Surg.* **2023**, *45*, 34. [CrossRef] [PubMed]
22. Toia, M.; Stocchero, M.; Jinno, Y.; Herath, M.; Galli, S.; Papia, E.; Ahmad, M.; Becktor, J.P. Inter-implant distance correlated to different preparation protocol on cortical bone: An animal study. *BMC Oral Health* **2025**, *25*, 1512. [CrossRef] [PubMed]
23. Zamparini, F.; Gandolfi, M.G.; Spinelli, A.; Ferri, M.; Iezzi, G.; Botticelli, D.; Prati, C. Mineralization and morphology of peri-implant bone around loaded and unloaded dental implants retrieved from the human mandible. *Oral Maxillofac. Surg.* **2023**, *28*, 623–637. [CrossRef] [PubMed]
24. Cafferata, E.A.; Schwarz, F.; Gruber, R. Antiresorptive therapy influence on peri-implant diseases: Clinical implications and osteoimmunological perspectives. *Periodontology 2000* **2026**, *online ahead of print*. [CrossRef] [PubMed]
25. Anitua, E.; Alkhraisat, M.H.; Eguia, A. On Peri-Implant Bone Loss Theories: Trying to Piece Together the Jigsaw. *Cureus* **2023**, *15*, e33237. [CrossRef] [PubMed]
26. Parle, E.; Tio, S.; Behre, A.; Carey, J.J.; Murphy, C.G.; O'Brien, T.F.; Curtin, W.A.; Kearns, S.R.; McCabe, J.P.; Coleman, C.M.; et al. Bone Mineral Is More Heterogeneously Distributed in the Femoral Heads of Osteoporotic and Diabetic Patients: A Pilot Study. *JBMR Plus* **2019**, *4*, e10253. [CrossRef] [PubMed]
27. Boivin, G.; Farlay, D.; Bala, Y.; Doublier, A.; Meunier, P.J.; Delmas, P.D. Influence of remodeling on the mineralization of bone tissue. *Osteoporos. Int.* **2009**, *20*, 1023–1026. [CrossRef] [PubMed]
28. Acharya, A.; Sahai, R.; Ravindra, K.A.; Mishra, S.; Uikey, G.; Electricwala, M.M. Comparative Study on the Effect of Various Implant-Abutment Connections on Microbial Leakage. *J. Pharm. Bioallied Sci.* **2025**, *17*, S1307–S1309. [CrossRef] [PubMed]
29. Baj, A.; Bolzoni, A.; Russillo, A.; Lauritano, D.; Palmieri, A.; Cura, F.; Silvestre, F.J.; Gianni', A. Cone-morse implant connection system significantly reduces bacterial leakage between implant and abutment: An in vitro study. *J. Biol. Regul. Homeost. Agents* **2017**, *31*, 203–208. [PubMed]
30. Ting, M.; Huynh, B.H.; Woldu, H.G.; Gamal, I.; Suzuki, J.B. Clinical Impact on Dental Implant Survival in Patients Taking Antiresorptive Medications: A Systematic Review and Meta-Analysis. *J. Oral Implantol.* **2023**, *49*, 599–615. [CrossRef] [PubMed]
31. Brauner, E.; Valentini, V.; Romeo, U.; Cantore, M.; Laudoni, F.; Rajabtork Zadeh, O.; Formisano, V.; Cassoni, A.; Della Monaca, M.; Battisti, A.; et al. Dental Implant Failure Risk in Post Oncological Patients, a Retrospective Study and Sapienza Head and Neck Unit Decisional Protocol- 7 Years of Follow-Up. *Diagnostics* **2022**, *12*, 1863. [CrossRef] [PubMed]
32. Perussolo, J.; Donos, N. Maintenance of peri-implant health in general dental practice. *Br. Dent. J.* **2024**, *236*, 781–789. [CrossRef] [PubMed]
33. Wang, H.L.; Avila-Ortiz, G.; Monje, A.; Kumar, P.; Calatrava, J.; Aghaloo, T.; Barootchi, S.; Fiorellini, J.P.; Galarraga-Vinueza, M.E.; Kan, J.; et al. AO/AAP consensus on prevention and management of peri-implant diseases and conditions: Summary report. *J. Periodontol.* **2025**, *96*, 519–541. [CrossRef] [PubMed]
34. Ortiz-Echeverri, A.M.; Gallego-González, C.; Castaño-Granada, M.C.; Tobón-Arroyave, S.I. Risk indicators associated with peri-implant diseases: A retrospective cross-sectional study of Colombian patients with 1 to 18 years of follow-up. *J. Periodontal Implant Sci.* **2023**, *54*, 161–176. [CrossRef] [PubMed]
35. Bardis, D.; Agop-Forna, D.; Pelekanos, S.; Chele, N.; Dascălu, C.; Török, R.; Török, B.; Cristea, I.; Bardi, P.M.; Forna, N. Assessment of Various Risk Factors for Biological and Mechanical/Technical Complications in Fixed Implant Prosthetic Therapy: A Retrospective Study. *Diagnostics* **2023**, *13*, 2341. [CrossRef] [PubMed]
36. Cheng, Y.C.; Ewers, R.; Morgan, K.; Hirayama, M.; Murcko, L.; Morgan, J.; Bergamo, E.T.P.; Bonfante, E.A. Antiresorptive therapy and dental implant survival: An up to 20-year retrospective cohort study in women. *Clin. Oral Investig.* **2022**, *26*, 6569–6582. [CrossRef] [PubMed]
37. Crupi, A.; Lanzetti, J.; Todaro, D.; Pera, F.; Erovigni, F.M. Dental Implant Survival and Risk of Medication-Related Osteonecrosis in the Jaws in Patients Undergoing Antiresorptive Therapy: A Systematic Review. *Int. J. Mol. Sci.* **2025**, *26*, 3618. [CrossRef] [PubMed]
38. Roy, R.; Chopra, A.; Karmakar, S.; Bhat, S.G. Applications of Artificial Intelligence (AI) for Diagnosis of Periodontal/Peri-Implant Diseases: A Narrative Review. *J. Oral Rehabil.* **2025**, *52*, 1193–1219. [CrossRef] [PubMed]
39. Fanelli, F.; Tisci, A.; Lo Muzio, L.; Troiano, G.; Caponio, V.C.A.; Dioguardi, M.; Zhurakivska, K. Artificial Intelligence for Radiographic Diagnosis of Peri-Implantitis: A Comprehensive Review on Detection, Measurement, and Risk Stratification. *J. Clin. Med.* **2026**, *15*, 5210. [CrossRef] [PubMed]
40. Mugri, M.H. Accuracy of Artificial Intelligence Models in Detecting Peri-Implant Bone Loss: A Systematic Review. *Diagnostics* **2025**, *15*, 655. [CrossRef] [PubMed]

Disclaimer/Publisher's Note: The statements, opinions and data contained in all publications are solely those of the individual author(s) and contributor(s) and not of MDPI and/or the editor(s). MDPI and/or the editor(s) disclaim responsibility for any injury to people or property resulting from any ideas, methods, instructions or products referred to in the content.